Numerical Study on the Validity of the Taylor Hypothesis in Space Plasmas

Silvia Perri[1], Sergio Servidio[1], Andris Vaivads[2], and Francesco Valentini[1]
[1] Dipartimento di Fisica, Università della Calabria, Via P. Bucci, I-87036 Rende, Italy; silvia.perri@fis.unical.it
[2] Swedish Institute of Space Physics, Uppsala, Sweden

Abstract

In situ heliospheric measurements allow us to resolve fluctuations as a function of frequency. A crucial point is to describe the power spectral density as a function of the wavenumber, in order to understand the energy cascade through the scales in terms of plasma turbulence theories. The most favorable situation occurs when the average wind speed is much higher than the phase speed of the plasma modes, equivalent to the fact that the fluctuations' dynamical times are much longer than their typical crossing period through the spacecraft (frozen-in Taylor approximation). Using driven compressible Hall-magneothydrodynamics simulations, in which an "imaginary" spacecraft flies across a time-evolving turbulence, here we explore the limitations of the frozen-in assumption. We find that the Taylor hypothesis is robust down to sub-proton scales, especially for flows with mean velocities typical of the fast solar wind. For slow mean flows (i.e., speeds of the order of the Alfvèn speed) power spectra are subject to an amplitude shift throughout the scales. At small scales, when dispersive decorrelation mechanisms become significant, the frozen-in assumption is generally violated, in particular for k-vectors almost parallel to the average magnetic field. A discussion in terms of the spacetime autocorrelation function is proposed. These results might be relevant for the interpretation of the observations, in particular for existing and future space missions devoted to very high-resolution measurements.

Key words: interplanetary medium – methods: numerical – plasmas – turbulence

1. Introduction

Since the first pioneering spacecraft observations, the interplanetary medium has appeared to be characterized by a distribution of kinetic and magnetic energy decaying as a power law, going from long to short timescales (Coleman 1968). This evidence is profoundly analogous to turbulence in non-magnetized fluids, where the energy is transferred from large to small scales, at which it eventually dissipates. The energy cascade, usually interpreted using the power spectral density (PSD) of velocity fluctuations, follows, in ordinary fluids, a power law $PSD(k) \propto k^{-5/3}$ at intermediate scales (Kolmogorov 1941). Spacecraft data have highlighted the presence of a similar power law in frequencies $PSD(f) \propto f^{-5/3}$, both for velocity and magnetic fluctuations. However, while in non-magnetized fluids experiments allow us to make spatial measurements and to derive the turbulence properties as a function of spatial scales (or wavevectors) (Anselmet et al. 1984; Kurien et al. 2001; Foucaut et al. 2004), single-satellite data permit us to collect information on the field properties only as a function of time.

In order to relate timescales to spatial scales, solar wind observations have usually been analyzed using the Taylor *frozen-in* hypothesis (Taylor 1938). Turbulent fluctuations at intermediate scales evolve typically at the Alfvèn speed $V_A = B_0/(4\pi\rho)^{1/2}$, which can be estimated once the mean field B_0 and the plasma density ρ are known. In the solar wind V_A is typically an order of magnitude smaller than the bulk speed (i.e., $V_{sw} \sim 400$–500 km s^{-1}), so fluctuations evolve over a time longer than the advection speed V_{sw} and can therefore be considered frozen-into the flow. In such cases, time variations can be associated with spatial variations. However, in a fully turbulent regime, the characteristic (evolution) times might be scale-dependent, and small scales might evolve faster, challenging the validity of the Taylor hypothesis.

Over the last 15 years, the launch of multispacecraft missions, such as *Cluster*, made up of four identical spacecraft in a tetrahedral configuration, has enabled the study of the spatial properties of turbulence in the solar wind and in the near-Earth environment, relaxing the use of the Taylor hypothesis (Sahraoui et al. 2009, 2010; Narita et al. 2010; Roberts et al. 2015; Perschke et al. 2016). More recently, the multi-satellite *Magnetospheric Multiscale* (*MMS*) mission has also permitted an in-depth and unprecedent determination of the spatial properties of turbulence in the near-Earth plasma, toward electron scales, reaching a very small (~ 10 km) interspacecraft separation (Burch et al. 2016; Graham et al. 2016; Yordanova et al. 2016). A multispacecraft method routinely applied to Cluster data is the k-filtering or wave telescope technique (Neubauer & Glassmeier 1990; Pinçon & Lefeuvre 1992; Motschmann et al. 1996). It is based on the assumption that turbulent fluctuations can be modeled as a superposition of randomly phased planes waves and it allows the estimation of the spectrum $PSD(\omega_{s/c}, \boldsymbol{k})$ that is a function of both the frequency in the spacecraft frame $\omega_{s/c} = 2\pi f$ and of the wavevectors. k-filtering has also been tested on a signal composed of random-phase plane waves and non-random coherent structures (Roberts et al. 2014).

Recently, observations have revealed that the solar wind is populated by zero-frequency structures, as thin current sheets, over a broad range of timescales (Perri et al. 2012; Greco et al. 2016; Perschke et al. 2016) beside almost oblique kinetic Alfvén waves (Sahraoui et al. 2010) and fast/whistler modes (Stawicki et al. 2001) recovered at scales smaller than the proton skin depth $d_i = c/\omega_{pi}$ (c is the light speed and ω_{pi} is the proton plasma frequency). The dispersion relation computed using the k-filtering method on Cluster intervals has confirmed the presence of a significant low-frequency population, over a broad range of wavenumbers (Roberts et al. 2015; Perschke et al. 2016). This zero-frequency (non-propagating) mode,

which is at odds with the concept of dispersion relations (Pezzi et al. 2017), might be the component of energy due to coherent structures, such as vortices, flux ropes, and small-scale current sheets associated with reconnection. Such a rich variety of structures might represent a crucial component of turbulence, playing a favorable role in the applicability of the Taylor hypothesis.

The aim of the present work is to study the validity of the frozen-in method in direct numerical simulations of space plasma turbulence, in order to make predictions useful for spacecraft observations. More specifically, we test under which plasma condition, and at which scales, the Taylor hypothesis can be considered a good approximation.

2. The Frozen-in Hypothesis

The use of single-spacecraft measurements implies that the proper frequencies of the plasma, which is in relative motion with respect to the satellite, are shifted in the spacecraft frame as (Taylor 1938)

$$\omega_{s/c} = \omega + \boldsymbol{k} \cdot \boldsymbol{V}_{sw}, \tag{1}$$

ω being the frequency in the plasma frame and $\boldsymbol{k} \cdot \boldsymbol{V}_{sw}$ being the advection term, that is, the projection of each wavevector associated with a spatial mode along the flow direction (Jian et al. 2009; Howes et al. 2014; Klein et al. 2014). Note that, in principle, the frequency in the plasma frame can be scale-dependent, namely $\omega = \omega(k)$. In Alfvènic turbulence, the typical speed associated with turbulent fluctuations is the Alfvèn speed, which in the solar wind at 1 au is $V_A \sim 50\,\mathrm{km\,s^{-1}}$. In such a case $V_A \ll V_{sw}$, so a reasonable approximation is $|\omega| \ll |\boldsymbol{k} \cdot \boldsymbol{V}_{sw}|$ and turbulent fluctuations do not dynamically evolve during the transit time of the plasma flow through the spacecraft position. Thus, they can be considered frozen-into the solar wind. From Equation (1), $\omega_{s/c} \sim \boldsymbol{k} \cdot \boldsymbol{V}_{sw}$, and the transformation from frequencies (time measurements) to wavenumbers (spatial measurements) is straightforward.

The case of slow mean flows (that is the, case where the plasma bulk speed is comparable to the speed of the fluctuations) is more problematic. In these regimes the frozen-in approximation can be violated (Perri & Balogh 2010; Klein et al. 2014). In particular, the advection term in Equation (1) becomes comparable to the frequency in the plasma frame, making it impossible to disentangle the contribution to the spacecraft frequency from the two terms on the right side of Equation (1). In typical conditions of slow streams, the PSD can be shifted toward higher frequencies than those in the cases where the Taylor hypothesis is fulfilled (see Figure 1 in Klein et al. 2014). Another possible condition for the violation of the frozen-in approximation is the presence of fast/dispersive waves in space plasmas. Klein et al. (2014) have shown how a linear superposition of whistler modes modifies the PSD at high frequency, leading to a flattening in the spectrum. Indeed, in such a case the plasma frame frequency of the modes grows more than linearly in k, while the advection term grows linearly. At large k (small scales) ω eventually dominates over $\boldsymbol{k} \cdot \boldsymbol{V}_{sw}$ in Equation (1), changing the shape of PSD at large k. This picture remains to be validated in more realistic time-dependent simulations of turbulence, where relations between time- and spatial-fluctuations remain poorly understood.

We propose to investigate the limits of validity of the frozen-in hypothesis in self-consistent simulations where both coherent structures and wave modes can be generated by the dynamical evolution of the system. In particular, we solved numerically the equations of compressible Hall magnetohydrodynamics (CHMHD), in 2.5 dimensions (2D in space and 3D in components of the fields). This choice has been motivated by the fact that in fluid-dispersive models the fast-dispersive modes are undamped (Gary & Borovsky 2004), thus generating very fast fluctuations. This scenario can be considered as an upper bound limit to Equation (1). Furthermore, the choice of 2D is motivated by the possibility of achieving higher Reynolds numbers and extended spectra.

3. Numerical Simulations

The numerical code used in our analysis is based on the CHMHD equations, as described in Vasconez et al. (2015). The equations can be written in dimensionless units as

$$\frac{\partial \rho}{\partial t} = -\boldsymbol{\nabla} \cdot (\rho \boldsymbol{v}), \tag{2}$$

$$\frac{\partial \boldsymbol{v}}{\partial t} = -(\boldsymbol{v} \cdot \boldsymbol{\nabla})\boldsymbol{v} + \frac{1}{\rho}[(\boldsymbol{\nabla} \times \boldsymbol{B}) \times \boldsymbol{B}]$$
$$- \frac{\beta}{2\rho}\boldsymbol{\nabla}(\rho T) - \nu_4 \nabla^4 \boldsymbol{v}, \tag{3}$$

$$\frac{\partial \boldsymbol{B}}{\partial t} = \boldsymbol{\nabla} \times \left[\boldsymbol{v} \times \boldsymbol{B} - \frac{\epsilon_H}{\rho}(\boldsymbol{\nabla} \times \boldsymbol{B}) \times \boldsymbol{B} \right] - \eta_4 \nabla^4 \boldsymbol{B}, \tag{4}$$

$$\frac{\partial T}{\partial t} = -(\boldsymbol{v} \cdot \boldsymbol{\nabla})T - (\gamma - 1)(\boldsymbol{\nabla} \cdot \boldsymbol{v})T - \chi_4 \nabla^4 T, \tag{5}$$

where ρ is the density, $\boldsymbol{u}$ is the bulk velocity, $\boldsymbol{B}$ is the (total) magnetic field, T is the temperature, $\gamma = 5/3$ is the adiabatic index, and the coefficients ν_4, η_4, and χ_4 are fictitious viscous coefficients. The latter terms have been introduced to dissipate the turbulent cascade, using hyperviscous dissipation, and are not intended to mimic any specific physical process. For these simulations, in order to limit the effect of dissipation at very high k-vectors, we used $\nu_4 = \eta_4 = \chi_4 \sim 10^{-6}$.

The equations have been normalized using large-scale Alfvénic units and the box length through large-scale energy containing lengths, in a square of size $2\pi L_0$. Both velocity and total magnetic fields have been normalized to the Alfvèn velocity, and the time has been normalized to the Alfvén time. The plasma beta β is defined as the ratio between the kinetic and the magnetic pressure, $\beta = P_0/(B_0^2/(4\pi\rho_0))$ (P_0 is the kinetic pressure and ρ_0 is a characteristic density). Using the large-scale normalization, ϵ_h is the so-called Hall parameter, the ratio between the proton skin depth d_i and the large-scale system size. For these simulations we set $\epsilon_H = 1/25$ and $\beta = 1$. The above equations have been solved in 2.5D and the magnetic field has been decoupled as $\boldsymbol{B} = \boldsymbol{B}_0 + \boldsymbol{\nabla}a \times \hat{\boldsymbol{z}}$, solving equations for the potential a and out-of-plane variances b_z. Equations (2)–(5) reduce to the ordinary MHD equations for a single compressible fluid in the limit $\epsilon_H \to 0$. The above set of nonlinear equations has been solved numerically with periodic boundary conditions. The CHMHD numerical code employs a Fourier pseudospectral method to calculate spatial derivatives, and time integration is performed via a second-order Runge–Kutta scheme. Aliasing errors in the evaluation of

Table 1
Parameters of the CHMHD Simulations

RUN	β	$\boldsymbol{B}_0$	Resolution
I	1	$(0, 0, 1)$	1024×1024
II	1	$\left(\cos\frac{\pi}{4}, 0, \sin\frac{\pi}{4}\right)$	512×512
III	0.4	$\left(\cos\frac{\pi}{4}, 0, \sin\frac{\pi}{4}\right)$	512×512

nonlinear terms are partially removed by a 2/3 truncation in the spectral space (Vasconez et al. 2015).

Each simulation has been performed for 25 Alfvèn times, driven at large scales. We initially let the system decay freely, and then we introduce a forcing at the peak of nonlinearity t^* [roughly the peak of the out-of-plane current $\langle j_z^2 \rangle$, here brackets denote spatial averages and $j_z = (\nabla \times \boldsymbol{B}) \cdot \hat{z}$]. The driving consists of a classical mode freezing, where only the amplitudes of the k-vectors in the range $1 < k \leqslant 4$ are retained as constant. Using Fourier transform, only the amplitudes are set as constant in time, leaving the phases free to evolve, in a natural way. This forcing allows long-duration steady-state turbulence without introducing extra characteristic times in the system, and injecting energy only at very large scales (Servidio et al. 2016). The statistics have been performed only in the steady-state range, namely for $5 \leqslant t \leqslant 25$. The rms value of the fluctuations, averaged over time, is $\delta b \sim \delta v \sim 0.5$. We have run three simulations where we have changed the mean field $\boldsymbol{B}_0$ configuration from being completely out-of-plane to lying in the $(x$–$z)$ plane and the plasma beta (see Table 1). Note that in RUN II and RUN III it is possible to study the violation of the frozen-in hypothesis in the presence of dispersive waves, such as whistler waves, propagating in the $(x$–$z)$ plane along $\boldsymbol{B}_0$ and in two different plasma conditions, i.e., $\beta = 1$ is the typical value found in the solar wind at 1 au and $\beta = 0.4$ can be considered as a more magnetized case.

In the steady-state regime of the simulations, fields are composed of characteristic structures, as can be observed in Figure 1(top). In that panel we show the contour plot of the plasma density ρ, for RUN I. The pattern is composed of vortical structures, as well as shock and thin filaments. This scenario is typical for all the simulations performed. In order to understand the statistical properties of turbulence we compute the PSD of the magnetic field. In the case of RUN I, since the magnetic field is out of the plane of the simulation, the in-plane fluctuations are homogeneous and isotropic. Because of that, in the range of the steady-state regime, we compute the time-averaged isotropic spectrum [averaging over time, and integrating in the (k_x, k_y) plane]. The PSD is reported in the bottom panel of Figure 1, where a well-developed inertial range can be recognized for wavenumbers $k > 4$ (associated with the typical scale of the forcing) and smaller than $k_i = 1/d_i$. At higher k-vectors, the spectrum slightly changes, first because of dispersive effects, and finally because of dissipation.

4. Virtual Spacecraft through Time-dependent Turbulence

In order to provide a useful numerical/theoretical tool for interpreting the single-satellite measurements in various plasma conditions, we allow a virtual spacecraft to "fly" across the simulation box as turbulence evolves in time. In particular, we set the angle θ in the (x, y) plane—the angle between the spacecraft trajectory and the x axis. The satellite increments its position by a $\Delta s = \Delta x/4$, Δx being the size along x of each
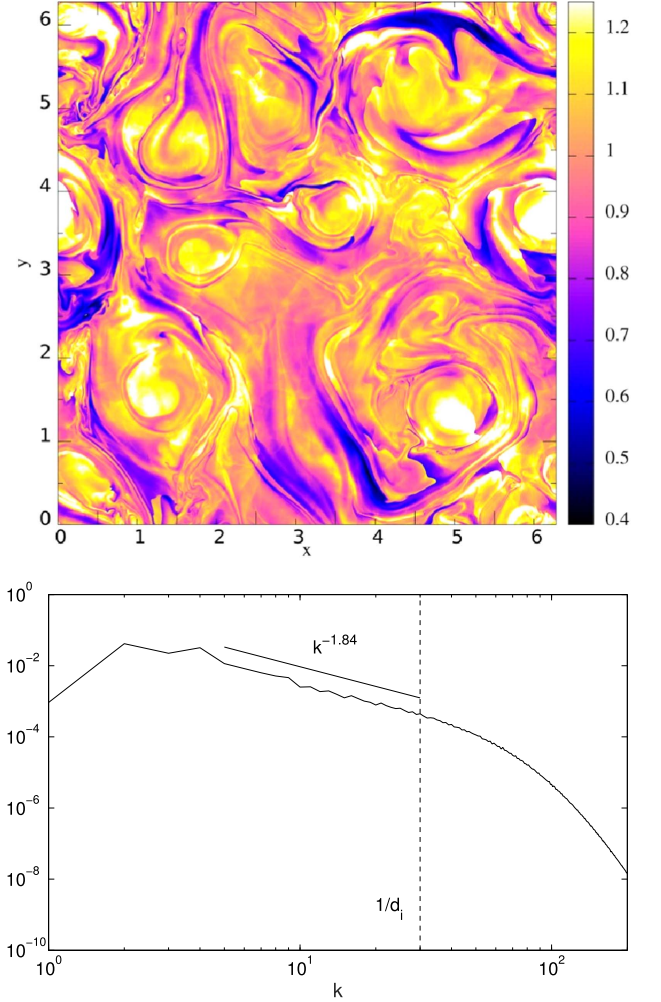
Figure 1. (Top) Contour plot of the plasma density in RUN I showing the formation of vortex-like structures as well as fast modes (compressive regions with sharp gradients). (Bottom) Time-averaged PSD of the magnetic field in RUN I as a function of the wavenumber (isotropic spectrum). The vertical line denotes the proton skin depth wavenumber.

cell in the simulation box. Thus, the virtual satellite makes four steps inside each cell, measuring the magnetic field with high resolution. A parameter of this numerical study is the flying speed of the satellite. In analogy with solar wind missions, the speed of the satellite is much lower than the plasma bulk speed V_{sw}, so in the spacecraft frame the plasma is observed to flow at V_{sw}. In the simulation we set such a condition, that is, the virtual spacecraft "observes" the fields flying at a speed that corresponds to the plasma bulk speed and with a time resolution $\Delta t = \Delta s/V_{sw}$.

Turbulence is evolving and we want the spacecraft to catch this dynamical evolution. In order to do so, beside a spatial interpolation of the fields along the spacecraft trajectory within the 2D plane, we also interpolate the spacecraft trajectory in time, between times t_i and t_{i+1}. Note that we sample the time cadence to be very high, in order to capture possible high-frequency effects. A cartoon of this procedure is displayed in Figure 2, where the spacecraft "measures" the magnetic fields across simulation planes, which are snapshots at various times, while also moving spatially. Basically, the procedure interpolates the magnetic fields both in space and in time. In summary, the spacetime trajectory of the satellite consists of a
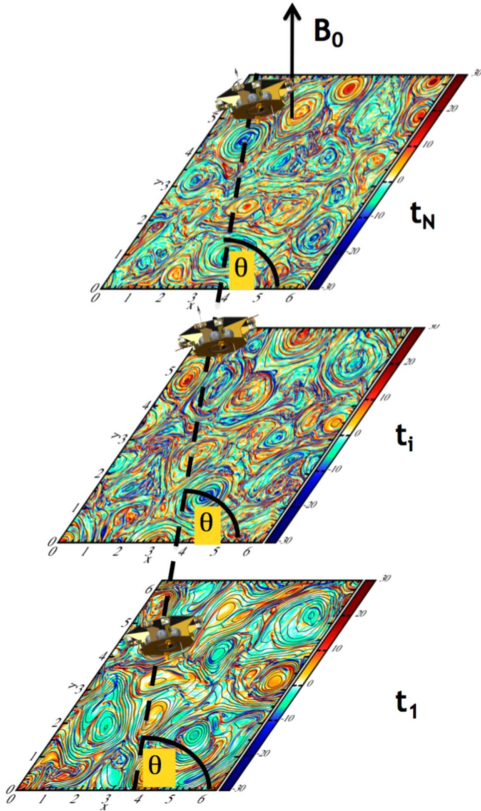
Figure 2. Cartoon of the procedure implemented to allow a synthetic spacecraft to fly at a given speed within the simulation box. The virtual spacecraft flies through simulation planes, which are different instants of plasma turbulence. θ is the angle in the spatial domain with the x axis.

double interpolation in a 3D box, 2D in space and 1D in time, as can be evinced from Figure 2.

4.1. Wavevectors **k**'s Perpendicular to **B**$_0$ (RUN I)

The first investigation of the limit of validity of the Taylor hypothesis has been performed by setting $\tilde{\boldsymbol{B}}_0 = (0, 0, 1)$ and $\theta = 80°$. Note that in RUN I the results do not depend on the angle θ between the virtual spacecraft trajectory and the x axis, since the turbulence is isotropic in the x–y plane. Examples of the time series measured by the virtual spacecraft flying at speeds $V_{sw} = 20V_A$, a typical condition for the fast solar wind, and $V_{sw} = 5V_A$, which is typical of very slow wind and magnetospheric flows, are shown in Figure 3. Note that the high-speed flow time series (black line) is characterized by a more rapid sequence of structures in the signal. The analysis of the violation of the frozen-in hypothesis is made by comparing the PSD computed from the artificial satellite time series (i.e., $\mathrm{PSD}_{s/c}$) with the exact spectrum computed from the simulation, i.e., one calculates $\mathrm{PSD}_{sim}(\boldsymbol{k}, t)$ with $\omega = 2\pi f = 2\pi/t$, and averaging over times, $\mathrm{PSD}_{sim}(\boldsymbol{k}) = \frac{1}{T}\int_{t_0}^{t_0+T}\mathrm{PSD}(\boldsymbol{k}, t')dt'$ (as reported in Figure 1). The $\mathrm{PSD}_{s/c}$ of the magnetic field time series has been estimated via a Welch method with 50% overlapped windows.

In this work we present the trace of the spectral matrices in the various cases analyzed. The left panel in Figure 4 reports the comparison between the exact spectrum from simulations (blue dashed lines) and the PSD of the magnetic field for three time series detected at three different speeds, that is $V_{sw} = 0.5V_A$, $5V_A$, $20V_A$ (black lines). The exact PSD has been
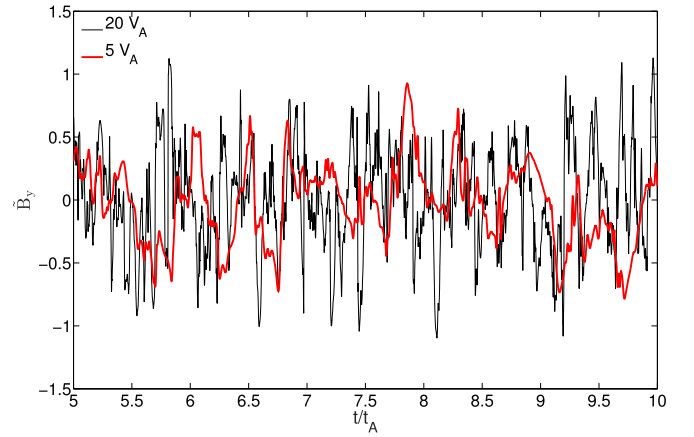

Figure 3. Magnetic field fluctuations as a function of the normalized simulation time, for a speed typical of solar wind plasma (black line) and for a speed comparable with magnetospheric flows (red line). See the text for further details.

computed from the simulation as an isotropic omnidirectional spectrum, averaging over the entire steady-state of the driven regime. Regarding the virtual spacecraft, in order to make this comparison feasible, the PSD for the magnetic field time series has been transformed such that $f \rightarrow k = 2\pi f/V_{sw}$ and $\mathrm{PSD}_{s/c}(f) \rightarrow \mathrm{PSD}_{s/c}(k) = \mathrm{PSD}_{s/c}(f)V_{sw}/2\pi$. The departure from the exact spectrum is clear for very slow flows, namely $V_{sw} = 0.5V_A$, over all scales. However, in order to better appreciate such a deviation, the right panel in Figure 4 compares the ratio between the spectrum computed from the virtual satellite time series $\mathrm{PSD}_{s/c}$ and the exact spectrum PSD_{sim}, for both slow (black line) and fast (red line) speeds. The red curve ($V_{sw} = 20V_A$) oscillates for almost all the range of scales around 1, while the black curve ($V_{sw} = 0.5V_A$) is always greater than 1 with a stronger deviation for $k > 50$. This result is in agreement with the predictions made by Klein et al. (2014) for a turbulence modeled as a superposition of Alfvènic modes; in this case there are no dispersive effects and only the slow flow condition leads to a violation of the Taylor hypothesis. The Hall-MHD simulation with an out-of-plane mean field is very close to an Alfvènic turbulence, where zero-frequency coherent structures (such as current sheets and vortices), emerging in the plasma, tend to better obey the frozen-in hypothesis. It is important to notice, indeed, that the dispersive phenomena affect the dynamics at scales considerably smaller than the proton skin depth, at variance with the dispersion relation expectations. The general picture is consistent with coherent structures slowing down the Eulerian fluctuations, reducing the violation effect.

4.2. Wavevectors **k**'s Oblique with Respect **B**$_0$ (RUN II and III)

The second set of simulations has been done by tilting the mean field direction of $\phi = 45°$ with respect to the x axis. This allows us to sample along the x direction possible wave-propagation effects. The virtual spacecraft path has been set to have $\theta = 5°$, in order to be almost aligned with one component of the mean field, and $\theta = 85°$ for the perpendicular flight. In such a case the component of $\boldsymbol{B}_0$ along x adds anisotropy in the x–y plane. To evaluate the exact time-averaged spectrum for the anisotropic simulation, first we obtain the 2D spectrum as a function of time, $\mathrm{PSD}(k_x, k_y, t)$. Then, we move to a new
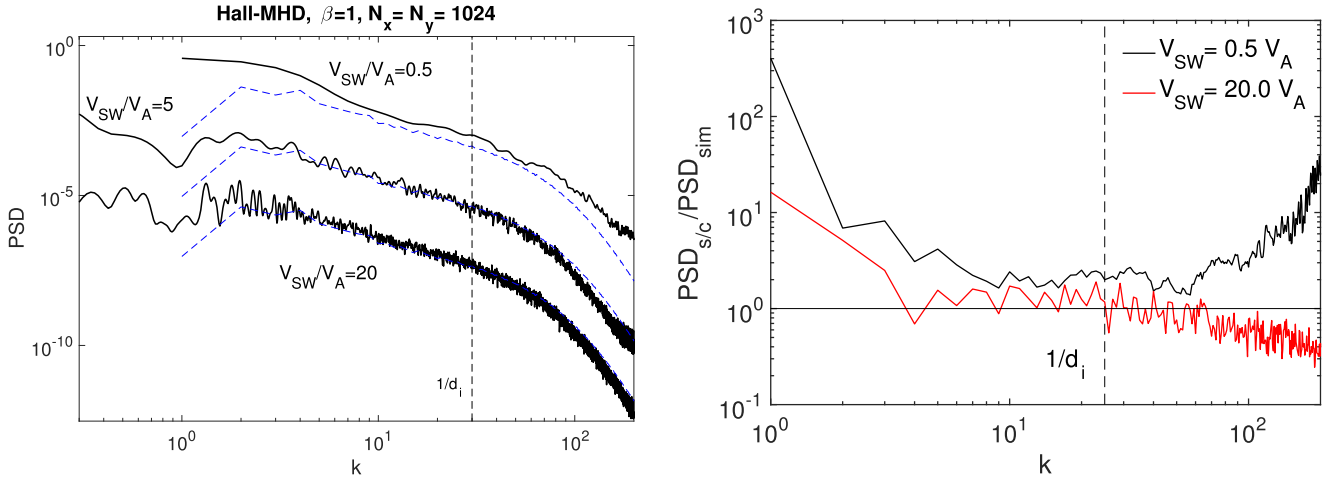
Figure 4. (Top) Comparison between the exact spectrum from simulations (blue dashed lines) and the PSD of the magnetic field for three time series detected at three different speeds, that is $V_{sw} = 0.5V_A$, $5V_A$, $20V_A$ (black lines), in RUN I. Curves have been shifted for readability. (Bottom) Ratio between the spectrum computed from the virtual satellite time series $\mathrm{PSD}_{s/c}$ and the exact spectrum PSD_{sim} for both slow (black line) and fast (red line) speeds.

coordinate system, $\mathrm{PSD}(k_x, k_y, t) \rightarrow \mathrm{PSD}(k'_x, k'_y, t)$, by rotating the Cartesian axes counterclockwise by an angle θ. The new spectrum is obtained through a 2D interpolation, and the k'_x axis now points toward the satellite sampling direction $\hat{s}$. Finally, the exact (reduced) power spectrum, averaged over time, is obtained as $\mathrm{PSD}_{sim}(k) = \frac{1}{T} \int_{t_0}^{t_0+T} dt \int_{k'_y} dk'_y \mathrm{PSD}(k, k'_y, t)$.

The configuration with a tilted $\boldsymbol{B}_0$ is closer to typical solar wind conditions, at 1 au, and can be used as predictor for single-satellite observations. Moreover, a comparison between the spectra coming from the virtual satellite's trajectories almost aligned to x and those quasi-perpendicular to x is necessary to better validate the dispersive effects. The closer the spacecraft's path is to the mean field component, the higher dispersive wave activity might break the frozen-in condition. Figure 5 is in the same format as the right panel of Figure 4, but shows RUN II. Each box displays $\theta = 5°$ (black line) and $\theta = 85°$ (red line) for three different spacecraft speeds. Spanning from very slow to fast flows (see Figure legend), the deviation from the exact spectrum is higher for $\theta = 5°$ and becomes very large for scales smaller than d_i (indicated by the vertical dashed line). The differences between the two trajectories tend to be suppressed for fast flows, although the violation of the Taylor hypothesis remains substantial over all the ranges of scales and increases for $k > 1/d_i$. We can actually observe that even in fast flows the PSD from the time series detected by the virtual spacecraft flying almost parallel to x deviates faster from PSD_{sim} at small scales than in the case with $\theta = 85°$, evidence that confirms a stronger effect of whistler modes.

The same analysis has been performed on Run III, which has a lower β (see Table 1). Figure 6 shows the ratio between the spectrum observed by the virtual spacecraft and the exact spectra in RUN II and RUN III, for $V_{sw} = 5V_A$ and $\theta = 5°$— the most extreme configuration. In RUN II and RUN III, the spectrum observed by the virtual satellite deviates from the exact spectrum over a broad range of scales, and a weak influence from the plasma β is observed. In order to interpret this result, we computed, by means of a standard two-fluid linear solver, the dispersion relations for the two cases, from

linear Hall-MHD theory, for a plasma having $\boldsymbol{k}$ tilted by $\phi = 45°$ with respect to $\boldsymbol{B}_0$. The inset of Figure 6 displays the phase speed as a function of the wavenumber for fast, Alfvènic, and slow modes in a $\beta = 0.4$ (red dashed lines) and a $\beta = 1$ (black lines) scenario. When $\beta = 1$, for $k < 1/d_i$, the fast and slow modes travel slightly faster than in the lower beta case. On the other hand, at $k > 1/d_i$, the phase speed of Alfvènic modes becomes substantially higher for $\beta = 1$ than in $\beta = 0.4$. Overall, the contributions from the three branches of the linear modes in the simulations lead to a slightly larger deviation from the Taylor hypothesis in RUN II, the phase speeds being generally higher. However, the presence of coherent, almost zero-frequency structures tends to suppress the spectral differences between RUN II and RUN III.

It is important to understand the basic mechanism that breaks the Taylor hypothesis.

5. Decorrelation Mechanism and the Taylor Hypothesis

Turbulent fluctuations are typically broadband on spatial and temporal scales, while nonlinear couplings both generate and destroy correlations among fluctuations. These interactions may be of several types, such as local-in-scale nonlinear distortion of eddies, or the transport or "sweeping" of small eddies by the large eddies (Chen & Kraichnan 1989), and finally, the fast/dispersive evolution of perturbations. The observed PSDs are consistent with local scale-to-scale transfer, dominated by nonlinearity. However, the physics of time decorrelation is distinct and depends on the advection (or sweeping) characteristic time at scale, defined as $\tau_{sweep}(k) = 1/(k\delta v)$. It has been demonstrated that this effect dominates the mode decorrelation in the inertial range of both hydrodynamic and MHD turbulence, as well as in anisotropic MHD turbulence (Chen & Kraichnan 1989; Servidio et al. 2011; Lugones et al. 2016). Here we will explore this issue in the case of CHMHD and establish a connection with the Taylor hypothesis.

The spacetime structure for a given turbulent vector field, e.g., the magnetic field $\boldsymbol{b}(\boldsymbol{x}, t)$, can be described by the two-point, two-time autocorrelation function $C(\boldsymbol{r}, \tau) = \langle \boldsymbol{b}(\boldsymbol{x}, t) \cdot \boldsymbol{b}(\boldsymbol{x} + \boldsymbol{r}, t + \tau) \rangle / \langle b^2 \rangle$, where the brackets indicate an adequate ensemble
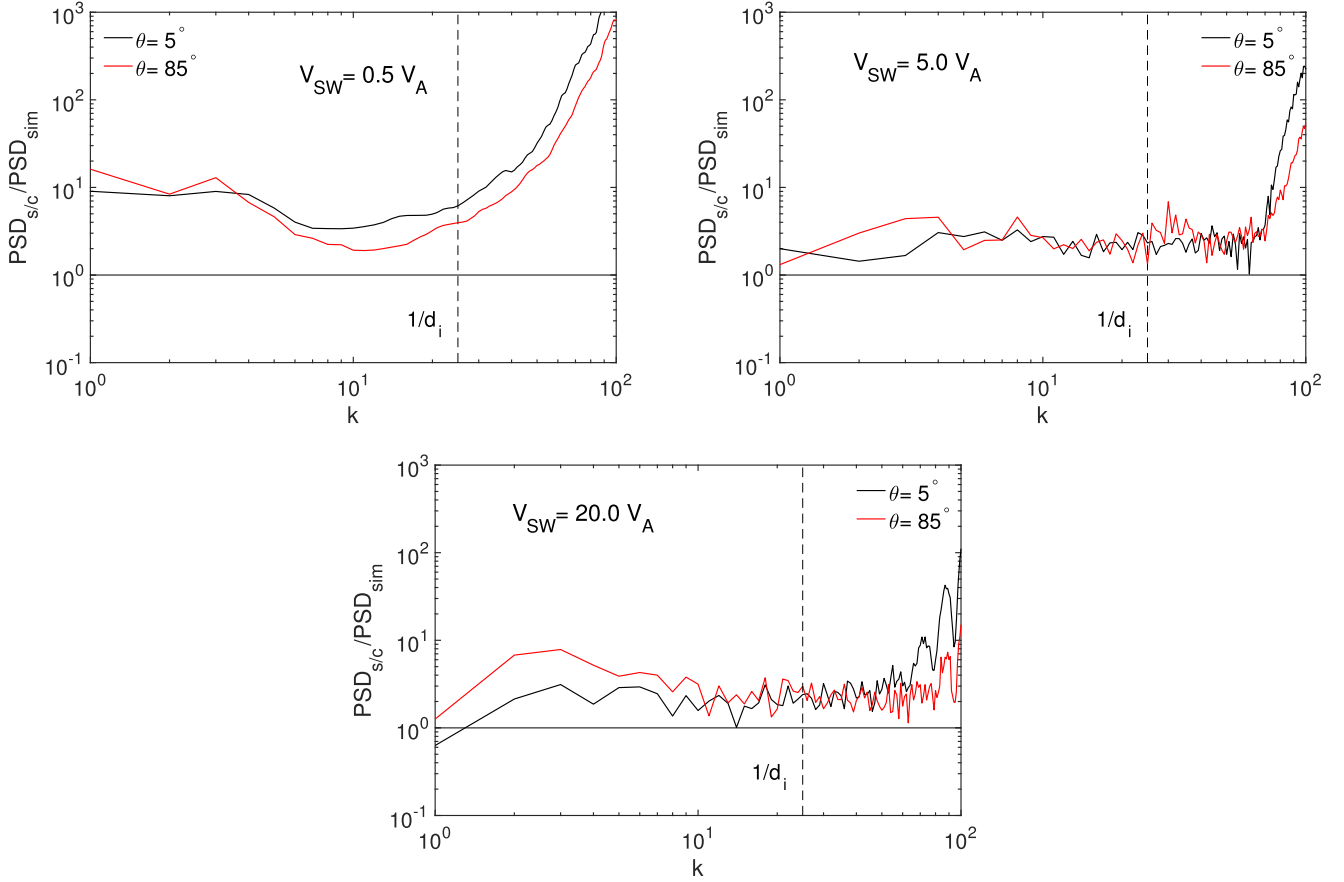
Figure 5. Ratio between the spectrum computed from the virtual satellite time series PSD$_{s/c}$ and the exact spectrum PSD$_{sim}$ for the spacecraft trajectory almost aligned to x (black line) and quasi-perpendicular to x (red line) in the case of RUN II. The panels refer to different wind speeds.
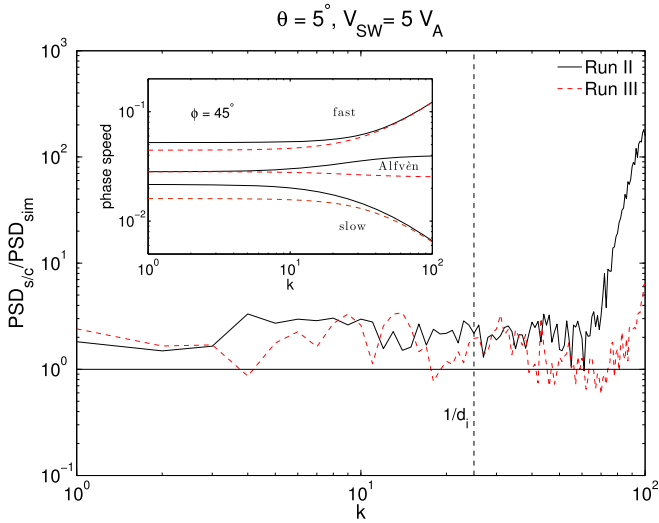
Figure 6. Ratio between the spectrum computed from the virtual satellite time series PSD$_{s/c}$ and the exact spectrum PSD$_{sim}$ for spacecraft trajectory almost aligned to x and for $V_{sw} = 5V_A$ for RUN II (black line) and RUN III (red dashed line). The inset shows the phase speeds in Alfvén units as a function of k for fast, Alfvénic, and slow modes in a $\beta = 1$ (black lines) and in a $\beta = 0.4$ (red dashed lines) plasma with a mean field tilted by $\phi = 45°$ with respect to $\boldsymbol{k}$.

(spatial and temporal) average and the denominator is the energy of the fluctuations. Fourier-transforming in r leads to the time-lagged spectral density, which can be normalized to the average

energy and therefore defined as

$$R(\boldsymbol{k}, \tau) = \frac{1}{2\langle|\tilde{\boldsymbol{b}}(\boldsymbol{k}, t)|^2\rangle_T} \times \langle \tilde{\boldsymbol{b}}(\boldsymbol{k}, t) \cdot \tilde{\boldsymbol{b}}^*(\boldsymbol{k}, t + \tau) + \tilde{\boldsymbol{b}}^*(\boldsymbol{k}, t) \cdot \tilde{\boldsymbol{b}}(\boldsymbol{k}, t + \tau)\rangle_T. \quad (6)$$

The function $R(\boldsymbol{k}, \tau)$ is the scale-dependent (or "filtered") correlation function. This propagator retains the main information about the spacetime behavior of the fluctuations and is of central importance in turbulence closure models. The time decorrelation mechanism can be identified by inspecting R as a function of τ and k.

The estimated correlation function $R(\boldsymbol{k}, \tau)$ is shown in Figure 7 for a selection of wavenumbers k, for simulation II. It is evident that in all cases the correlation approaches zero with a rate that depends on the wavevector k. The higher k's lose memory more rapidly than the lower k's, as predicted in Servidio et al. (2011). Note that we computed the correlation for an isotropic shell truncation (averaging on different k's) in order to enhance the statistics of the computation. In order to compute the correlation time $\tau_C(k)$ of each mode of turbulence, we used a simple e-folding technique (Matthaeus et al. 2016), as summarized in Figure 7 (horizontal line represents $1/e$).

As discussed before, a key issue is the scaling of correlation times $\tau_C(k)$ with wavenumber k, reported here in Figure 8. Using the measured correlation functions, we fit the correlation times as $\tau_C(k) \sim k^\alpha$, both in the inertial and in the dispersive-dissipative range. From the fit, we obtained $\alpha \sim -0.97$ in the
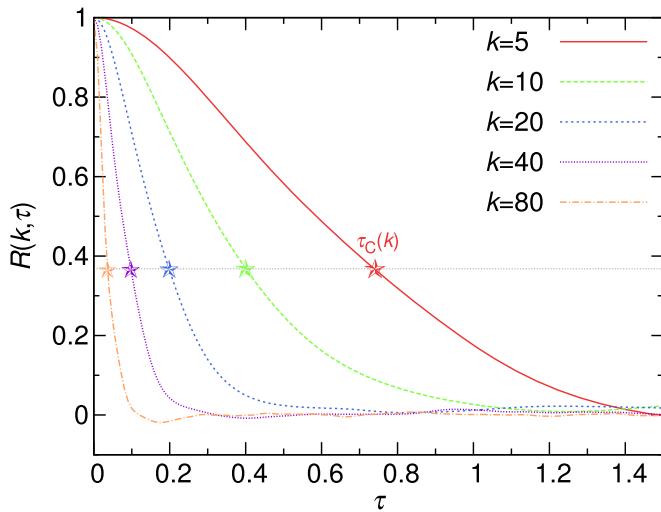
Figure 7. Correlation function $R(k, \tau)$ vs. time-lag τ, for different k (RUN II). The modes decorrelate in time as observed in hydrodynamics and incompressible MHD. The correlation time $\tau_C(k)$ (stars) can be computed as the e-folding time of the decorrelation mechanism.
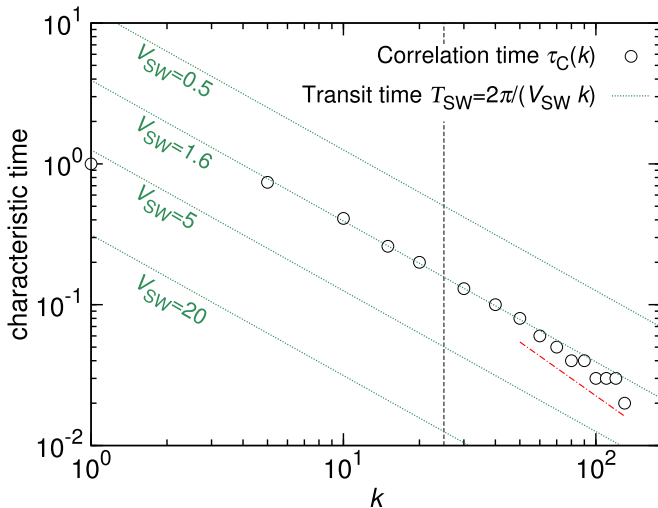
Figure 8. Correlation time $\tau_C(k)$ (open circles) as a function of k, obtained from the autocorrelation function in Figure 7. In the inertial range, $5 \leqslant k \leqslant 20$, the fit gives $k^{-0.97}$; at scales smaller than d_i^{-1}, $\tau_C \sim k^{-1.3}$ (red dotted-dashed line). The dashed (oblique green) lines represent the behavior of the transit solar wind time $T_{SW} = \frac{2\pi}{k V_{SW}}$, evaluated for different speeds. For a robust Taylor hypothesis, time must be much smaller than $\tau_C(k)$.

inertial range, in full agreement with the sweeping prediction (k^{-1}), where the dominating decorrelation mechanism is due to the random sweeping of eddies through the probe $\sim 1/(\delta b k)$.

At scales on the order (and smaller) of the proton skin depth, namely for $k > 2 d_i^{-1}$, the nature of the decorrelation mechanism changes, becoming substantially faster. In the secondary range the correlation time behaves as $\tau_C(k) \sim k^{-1.3 \pm 0.1}$. This change of decorrelation regime is very important for the spacetime "ambiguity" in single-spacecraft measurements, since it causes the Taylor hypothesis breakdown. In Figure 8, we also show the characteristic crossing time due to the solar wind flow, defined as $T_{SW}(k) = 2\pi/(V_{SW} k)$, varying the mean wind speed. In order to fulfill the Taylor hypothesis, this time should be much smaller than the decorrelation time of the fluctuations. This is true for $V_{SW} \gg 1.6 \delta v$. For large scales, $k \ll d_i^{-1}$, the mean flow gives only a shift, having the same

k-dependence of the sweeping time. At small scales, when the dispersive effects become important, the correlation time changes behavior, requiring a more strict constraint on the mean flow. More investigation on the nature of the small-scale regime is needed, especially at scales comparable to and smaller than the electron skin depth, using full kinetic models of plasma.

6. Discussions and Conclusions

We investigated, via 2.5D CHMHD simulations, the limit of validity of the Taylor frozen-in hypothesis, which is routinely used to interpret single-spacecraft measurements in space plasmas. The mean field configuration has been changed in order to both minimize and to include dispersive waves, so that $\boldsymbol{B}_0$ has been allowed to be out-of-plane and tilted with respect to the x axis. A virtual satellite has been launched, at various speeds, through the spacetime domain. Changing the synthetic spacecraft speed means exploring different plasma flow conditions, going from $V_{sw} \gg V_A$—a condition typical of the fast solar wind—to the case in which $V_{sw} \sim V_A$—which is more relevant for magnetospheric flows. In principle, this methodology can be applied to any model of plasma, in different dimensions, and including different effects (full kinetic physics, Larmor radius effects, electron and Debye length fluctuations, and so on.) Our study goes beyond the investigation of the Taylor hypothesis in the presence of only wave modes, retaining the presence of spontaneously generated structures that generally overpopulate the range of fluctuations with very small frequencies (much smaller than the Alfvén dispersion frequency kV_A). The main findings of this work can be summarized as follows.

1. In the presence of an out-of-plane mean field, dispersive effects are weak, and turbulence is more like a mixture of Alfvènic modes and zero-frequency coherent structures, with current sheets and vortices at different scales (see top panel in Figure 1). In this case we do not observe a substantial violation of the Taylor hypothesis, except for very low speeds, i.e., $V_{sw} = 0.5 V_A$. In this case the PSD is shifted in amplitude.

2. When the mean field is tilted by $\phi = 45°$ with respect to x, and satellites move along this direction, dispersive effects come into play and the Taylor hypothesis is observed to be violated for any flow speed. The violation caused by dispersive effects is seen as a flattening in the PSD. Again, the violation is stronger for slow flows and increases for $k > 1/d_i$, but is less than that in a pure wave-dominated regime. The frozen-in hypothesis can be considered valid for $V_{sw} = 20 V_A$ (corresponding to fast solar wind flows).

3. A slight difference in the violation of the Taylor hypothesis has been found in RUN II ($\beta = 1$) and RUN III ($\beta = 0.4$) that can be explained from the influence of the plasma β on the phase speed of linear modes (see Figure 6). The phase speed is generally higher over a broad range of scales for $\beta = 1$, leading to a larger deviation of PSD$_{s/c}$ from PSD$_{sim}$.

4. A key role in the Taylor hypothesis is played by the presence of zero-frequency structures; indeed, in RUN II the discrepancy between PSD$_{sim}$ and PSD$_{s/c}$ seems to be less pronounced than that in the spectra reported in the right panel of Figure 3 of Klein et al. (2014). Furthermore, the deviation between PSD$_{sim}$ and PSD$_{s/c}$ changes slightly

with the plasma beta but not as much as we would expect if we had a superposition of linear modes only (according to the trend of the phase speed with k). We believe that this lower violation of the frozen-in condition can be due to the presence of zero-frequency structures in CHMHD, for which $\omega_{s/c} \sim \mathbf{k} \cdot \mathbf{V}_{sw}$.

5. An analysis of the full spacetime autocorrelation function reveals that the inertial range of fluctuations is dominated by sweeping effects, leading to just an amplitude shift for all the fluctuations with $k < d_i$. At smaller scales, the decorrelation time, namely the characteristic evolving time of each mode k, has a stronger dependence on k, requiring more restrictions on the solar wind mean speed. This may lead to an interpretation of the breakdown of the frozen-in condition, and of the consequent modification of the PSD, in terms of physical dynamical times.

We remark that compressible CHMHD can be seen as an extreme case, since magnetoacoustic and fast modes are undamped. This work can provide an upper bound to the validity of the frozen-in assumption. However, the present methodology can be easily used and applied to other systems, in other geometries and regimes, also exploring self-consistent models of plasma dynamics. A future extension of this work might be the study of 3D turbulence, with spacecraft flying in space and time, including the kinetic effects at electron scales. At these lengths, where eventually the turbulent cascade terminates, a very fast decorrelation mechanism might develop, competing with the formation of very small current sheets and vortices.

References

Anselmet, F., Gagne, Y., Hopfinger, E. J., & Antonia, R. A. 1984, JFM, 140, 63
Burch, J. L., Torbert, R. B., Phan, T. D., et al. 2016, Sci, 352, aaf2939
Chen, S., & Kraichnan, R. H. 1989, PhFl, 1, 2019
Coleman, P. J. 1968, ApJ, 153, 371
Foucaut, J. M., Carlier, J., & Stanislas, M. 2004, MeScT, 15, 1046
Gary, S. P., & Borovsky, J. E. 2004, JGRA, 109, A06105
Graham, D. B., Khotyaintsev, Yu. V., Norgren, C., et al. 2016, GeoRL, 43, 4961
Greco, A., Perri, S., Servidio, S., Yordanova, E., & Veltri, P. 2016, ApJL, 823, L39
Howes, G. G., Klein, K. G., & TenBarge, J. M. 2014, ApJ, 789, 106
Jian, L. K., Russell, C. T., Luhmann, J. G., et al. 2009, ApJL, 701, L105
Klein, K. G., Howes, G. G., & TenBarge, J. M. 2014, ApJL, 790, L20
Kolmogorov, A. N. 1941, DoSSR, 30, 301
Kurien, S., Aivalis, K. G., & Sreenivasan, K. R. 2001, JFM, 448, 279
Lugones, R., Dmitruk, P., Mininni, P. D., Wan, M., & Matthaeus, W. H. 2016, PhPl, 23, 112304
Matthaeus, W. H., Weygand, J. M., & Dasso, S. 2016, PhRvL, 24, 245101
Motschmann, U., Woodward, T. I., Glassmeier, K. H., Southwood, D. J., & Pinçon, J. L. 1996, JGR, 101, 4961
Narita, Y., Glassmeier, K. H., Sahraoui, F., & Goldstein, M. L. 2010, PhRvL, 104, 171101
Neubauer, F. M., & Glassmeier, K. H. 1990, JGR, 95, 19115
Perri, S., & Balogh, A. 2010, ApJ, 714, 937
Perri, S., Goldstein, M. L., Dorelli, J. C., & Sahraoui, F 2012, PhRvL, 109, 191101
Perschke, C., Narita, Y., Motschmann, U., & Glassmeier, K. H. 2016, PhRvL, 116, 125101
Pezzi, O., Parashar, T. N., Servidio, S., et al. 2017, JPlPh, 83, 705830108
Pinçon, J. L., & Lefeuvre, F. 1992, JATP, 54, 1237
Roberts, O. W., Li, X., & Jeska, L. 2014, GI, 3, 247
Roberts, O. W., Li, X., & Jeska, L. 2015, ApJ, 802, 2
Sahraoui, F., Goldstein, M. L., Belmont, G., Canu, P., & Rezeau, L. 2010, PhRvL, 105, 131101
Sahraoui, F., Goldstein, M. L., Robert, P., & Khotyaintsev, Y. V. 2009, PhRvL, 102, 231102
Servidio, S., Carbone, V., Dmitruk, P., & Matthaeus, W. H. 2011, EL, 96, 55003
Servidio, S., Haynes, C. T., Matthaeus, W. H., et al. 2016, PhRvL, 117, 095101
Stawicki, O., Gary, S.-P., & Li, H. 2001, JGR, 106, 8273
Taylor, G. I. 1938, RSPSA, 164, 476
Vasconez, C. L., Pucci, F., Valentini, F., et al. 2015, ApJ, 815, 7
Yordanova, E., Vörös, Z., Varsani, A., et al. 2016, GeoRL, 43, 5969